Air Pollution Remediation in a Fixed Bed Photocatalytic Reactor Coated with TiO_2

C. R. Esterkin, A. C. Negro, O. M. Alfano, and A. E. Cassano
INTEC, Instituto de Desarrollo Tecnológico para la Industria Química (Universidad Nacional del Litoral and CONICET)
Güemes 3450 (3000), Santa Fe, Argentina

DOI 10.1002/aic.10472
Published online June 1, 2005 in Wiley InterScience (www.interscience.wiley.com).

In a previous article, the modeling and experimental verification of the radiation field inside a reactor made of several TiO_2 coated, parallel, flat glass fiber meshes, bilaterally UV irradiated was accomplished. The degradation of trichloroethylene (TCE) in an air stream is studied using different values of the pollutant feed concentration, relative humidity and light intensity under operating conditions where kinetic control of the process is established. A kinetic model based on a reaction scheme that involves atomic chlorine as an active reaction intermediate is developed for describing concentration dependencies. It includes, explicitly, the effect of the absorbed light intensity on the rate. The interaction of the existing radiation field with the solid semiconductor to generate electrons, and holes in the reaction catalyst activation step is also modeled. All kinetic parameters are estimated from experiments. The obtained kinetic expression gives a first-order dependence with respect to the TCE concentration and accounts for a competitive effect of water vapor and TCE for the catalyst active sites. An additional important feature of the derived expression is its ability to represent both limiting cases concerning the dependence of the reaction rate with the irradiation rate; that is, order 1 or order 0.5, as well as all possible intermediate values. In fact, the equivalent dependence obtained in this work was 0.6, a value closer to the second case. The results show good agreement between predictions derived from the proposed kinetic expression and TCE experimental concentration data at the reactor's exit. The proposed reactor design provides a practical device for the treatment of contaminated air; it permits a fairly uniform irradiation of the catalytic meshes and a good ratio of the irradiated surface area with respect to the volume of the gaseous reacting mixture. With these features, rather high TCE conversions can be obtained. © 2005 American Institute of Chemical Engineers *AIChE J,* 51: 2298–2310, 2005
Keywords: air pollution remediation, photocatalytic reactor, fixed bed reactor, glass fiber meshes, titanium dioxide, trichloroethylene.

Introduction

In the past two decades, photocatalytic processes have received considerable attention due to their potential application in air and water pollution remediation. Titanium dioxide is the preferred catalyst because of its stability under a variety of operating conditions, low cost and lack of toxicity. The choice of the semiconductor catalyst defines the type of radiation that can be applied to initiate the reaction; thus with a band gap of 3.2 eV, a wavelength below 390 nm must be applied to generate electrons and holes in the solid. This is an indication that also solar light could be a suitable source of energy. Even if artificial illumination is employed, the lower practical wavelength limit is about 300 nm. At shorter wavelengths, low cost,

Correspondence concerning this article should be addressed to A. E. Cassano at acassano@ceride.gov.ar.

standard glass or plastic ware cannot be used. Moreover, absorption by the catalyst becomes so strong that puts severe limitations to the size of all practicable devices. Several reactor configurations have been proposed: slurry, fluidized and fixed beds, the last two options resulting from the difficulties associated with downstream catalyst separation in the first one. Among the technical possibilities for air remediation, different types of fixed bed reactors have been proposed: flat or curved walls, corrugated walls, monoliths, packed beds and reticulated configurations. Although gas phase applications seem to be the ones with better success in the market[1] research efforts have not paralleled the extensive proliferation of the scientific literature connected with studies performed in water environments; this statement is even truer in the case of research contributions aimed at modeling these fixed bed reactors. However, important contributions have been made by Raupp and coworkers. They presented a two-flux radiation model for an annular packed-bed photocatalytic reactor[2] that is an extension of the two-flux model for parallel-plate reactors proposed by Maruyama and Nishimoto.[3] Hossain and Raupp[4,5] described the radiation field in a monolith photocatalytic reactor using a theory based on radiation exchange between surfaces in channels. Finally, a reticulated foam photocatalytic reactor was proposed and solved with Monte Carlo simulation[6] and with a deterministic two-dimensional (2-D) heterogeneous model.[7] At the same time, a model for absorption by TiO_2 films in a corrugated-plate photocatalytic reactor was described by Zhang et al.[8] Later on, the radiation field in a fixed bed reactor having the titanium dioxide catalyst immobilized on an inert support and made by a set of parallel, flat glass fiber meshes was discussed by Esterkin et al.[9] In this reactor, UV radiation enters the reactor through transparent, acrylic windows. Irradiation can be produced from one or both sides of the reactor.

The performance of this reactor for the treatment of an air stream contaminated with a low concentration of trichloroethylene (TCE) is presented in this work. In this case, the glass fiber meshes are significantly different than the ones used in the previous study. The custom made meshes employed previously were replaced by commercial ones kindly provided by Enerzone, Inc. of Canada and originally designed for a water treatment equipment. Titanium dioxide has been immobilized on the glass mesh with a sol-gel technique. 32 mg of TiO_2 per gram of glass fiber mesh were measured. The characteristics of the supporting mesh are: surface void fraction 0.69 and surface mesh density 50 g/m^2. The aforementioned change affected the optical characteristics of the new reactor and obligated a new determination of its optical parameters.

The gas phase photocatalytic oxidation of trichloroethylene employing near UV radiation and titanium dioxide was studied by Dibble and Raupp.[10] They reported that the rate of degradation was affected by the initial TCE concentration, and the oxygen and water vapor concentrations, indicating very untypical reaction orders for the three concentration variables. A simple kinetic model for the same reaction was later on described by Upadhya and Ollis[11] to account for the TCE concentration and light intensity dependences of the rate. Based on the competition between the recombination of electrons and holes and the superficial reaction of the charge carriers with the substrate, they proposed a theoretical explanation for the existence of the reported relationships between the reaction order with respect to light intensity and the concentration of TCE. Wang et al.[12] studied the degradation of TCE in the gas phase employing 365 nm UV light over titanium dioxide supported on glass beads. They found a fractional order (0.61) for the light intensity dependence and that the concentration dependence with respect to TCE, and water vapor concentration was satisfactorily explained with a model based on the competitive adsorption of TCE and water molecules on the same catalyst sites. Amama et al.[13] reported the photocatalytic oxidation of TCE in humidified atmosphere in an attempt to explain the observed inhibitory effect of water vapor in the degradation rate. They proposed an atomic chlorine-propagated chain reaction mechanism to explain the observed rates, as well as part of inhibition produced by the water vapor. Competitive adsorption between humidity and TCE was the second factor that was found to influence the rate. Zhao et al.[14] provided additional evidences to support the chlorine-atom mediated mechanism proposed to explain the high reaction rates observed in the photocatalytic degradation of chlorinated hydrocarbons. The authors thought that chlorine is photocatalytically generated from TCE, starting a homogeneous, chain reaction degradation of TCE. They provided additional experimental evidences to the atomic chlorine reaction enhancement hypothesis. Kim and Hong[15] conducted similar studies to elucidate the reaction rate dependence with respect to the concentration of TCE, the water vapor content and the flux of ultraviolet light. They used titanium dioxide coated on the surface of a reactor tube as a catalyst, and found that the concentration dependencies could be well-explained with a Langmuir-Hinshelwood type of kinetics, and that the dependence of the rate with the photon flux was of the order 0.35 at medium irradiation rates and 0.90 at lower ones, a type of result that, with some variations, has been repeatedly reported before. Recently, working on the photocatalytic degradation of TCE, Amama et al.[16] have provided additional evidence concerning the decrease in reactivity when the relative humidity of the reacting mixture is increased. Demeestere et al.[17,18] have reported results indicating that TCE removal efficiencies are increased when low relative humidity (RH), low TCE inlet concentrations and high-gas residence time have been used. An important group of these observations can be satisfactorily explained with the model presented in this contribution.

Description of the Reactor

The photocatalytic reactor is a rectangular parallelepiped made of acrylic plastic. To describe the reactor geometyry consider a Cartesian coordinate system. The contaminated air flow moves from the bottom to the top along the z direction of the gap between the catalytic meshes that are flat surfaces located in y-z planes (Figure 1a). The reaction space can house up to six of these parallel plates along the direction x (commercial glass-fiber meshes coated with titanium dioxide and supported by an acrylic frame) as it is shown in Figure 1 a and b, and Figure 2. The parallel plates were tightly mounted on the plastic frames to minimize irregular channeling of the air flow through the reaction space. The optical characteristics of these meshes (particularly, transmission and reflection) are reported later; absorption by the catalyst is very strong below 330 nm, and decreases gradually when moving to higher wavelengths, to be nearly zero at 390 nm corresponding to the limit defined by the band gap of the semiconductor. Light goes inside the

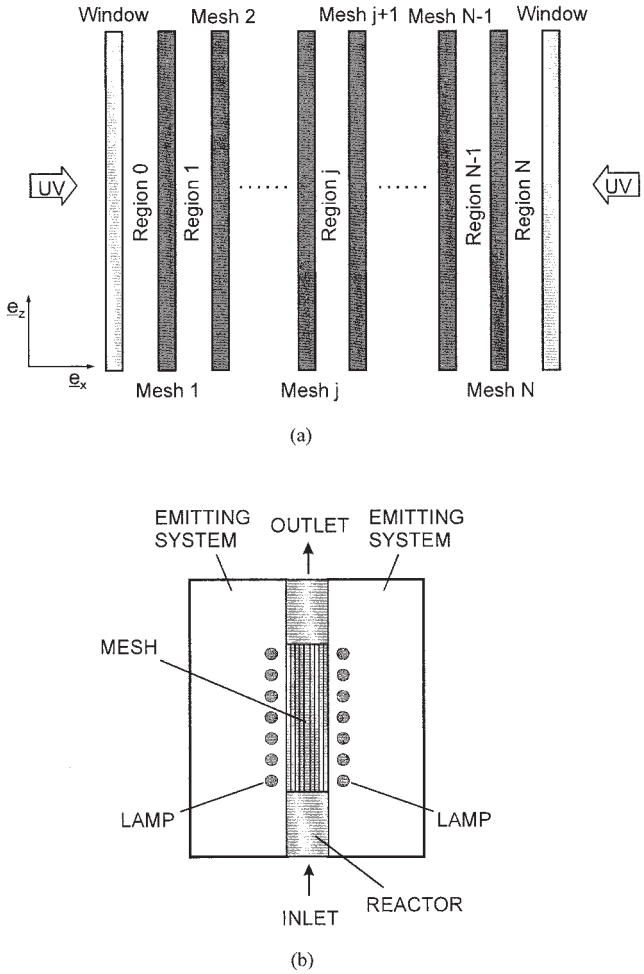

Figure 1. Photocatalytic reactor. (a) Reactor windows and meshes, and (b) photocatalytic reactor and emitting system.

reactor through rectangular windows made of an acrylic plastic, 3.2 mm thick. The particular brand employed in this work has a fairly good UVA transmission characteristics in the wavelength range between 290 and 390 nm. Transmittance and Reflectance of these plates were measured and reported before[9]

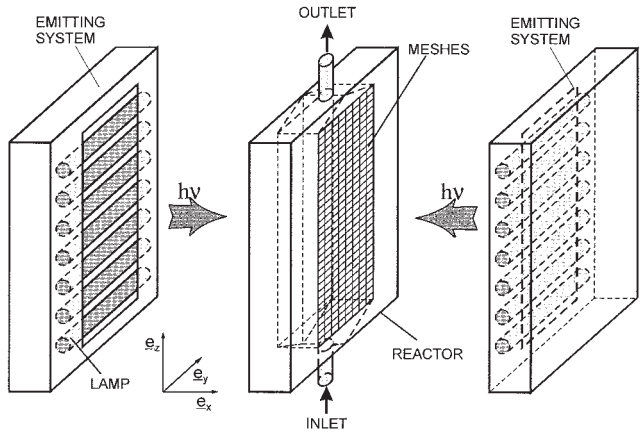

Figure 2. Photoreactor and emitting systems.

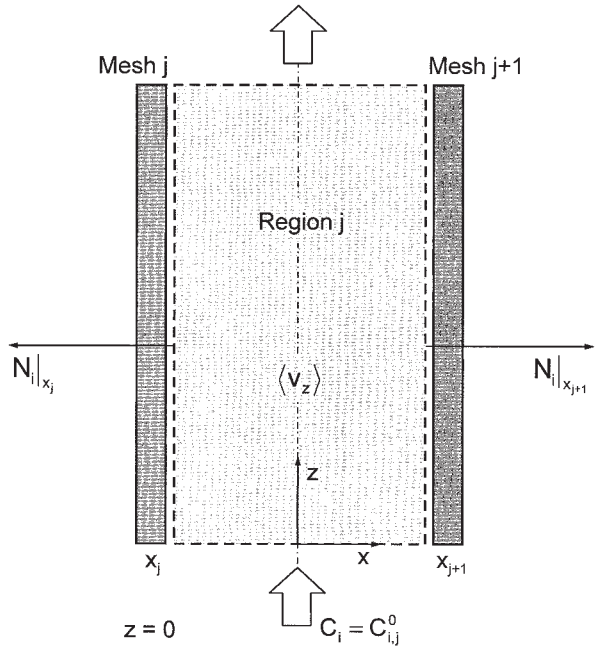

Figure 3. Mass balance in reactor region j between meshes j and j + 1.

(Figure 6a in the work of Esterkin et al.[9]). Each side of the reaction flat plate can be irradiated by a set of seven black-light lamps (Philips TL 4W/08 (F4T5/BLB)). These lamps have an emission that extends between 310 and 410 nm with a peak at 350 nm. Considering the radiation absorption range of the catalyst, the operation range of the reactor can be defined between 310 and 390 nm. At these wavelengths and above, trichloroethylene does not absorb radiation and, consequently, direct photolysis can be safely disregarded in the kinetic analysis of the experimental data. Each of the 14 lamps is connected to a command panel permitting the controlled operation of the whole illuminating system.

It can be noticed that the proposed photoreactor design show some features that makes it a convenient device from the efficiency point of view. Among them we can mention: (1) the employed meshes permitted to reach a reasonably high value for the ratio of illuminated catalytic area per unit volume of the reacting gas (the minimum value is 110 m^{-1}), (2) the adopted bilateral irradiation contributes to make the existing radiation field more uniform (results are shown in the last section of this contribution), and (3) the use of acrylic windows - transparent to radiation in the employed wavelength range - as a substitute for glass eliminates the risk of breakage, facilitates the reactor sealing and reduces costs.

Reactor Model

A simple reactor model is developed (Figure 3). No homogeneous reaction occurs in the gas phase, and convective flow exists only in the z direction ($v_x = v_y = 0$) with a velocity independent of z. With constant physical properties and under steady state conditions, the mass balance for the j-region located between meshes j and j+1 (Figure 1a) gives

$$v_z(\underline{x})\,\frac{\partial C_{i,j}(\underline{x})}{\partial z} - \mathcal{D}_{im}\underline{\nabla}^2 C_{i,j}(\underline{x}) = 0 \quad (i\text{: TCE}) \tag{1}$$

All surfaces perpendicular to the y direction are non permeable because they are not catalytic; hence, diffusive fluxes in the y direction are not considered. Diffusive fluxes in the z direction are neglected compared with the convective flow. Thus, the boundary conditions are

$$\begin{aligned} &z = 0 \quad C_{i,j} = C^0_{i,j} \\ &x = x_j \quad N_i\big|_{x_j} = -\mathcal{D}_{im}\,\frac{\partial C_{i,j}}{\partial x} \\ &x = x_{j+1} \quad N_i\big|_{x_{j+1}} = -\mathcal{D}_{im}\,\frac{\partial C_{i,j}}{\partial x} \end{aligned} \tag{2}$$

At any position z, Eq. 1 can be integrated in the cross sectional area of the generic reactor section j (Area = $\Delta x \times \Delta y$). Defining a velocity weighted concentration averaged over such an area $\langle C_{i,j}\rangle_{A_C}$, and an area averaged velocity $\langle v_z\rangle_{A_C}$

$$A_C\langle v_z\rangle_{A_C}\,\frac{d\langle C_{i,j}\rangle_{A_C}(z)}{dz} = \int_{A_C} \mathcal{D}_{im}\underline{\nabla}^2 C_{i,j}(\underline{x})\,dA = \oint_C \mathcal{D}_{im}\underline{\nabla} C_{i,j}\cdot\underline{n}\;ds \tag{3}$$

In Eq. 3, the Green's theorem in the plane has been used. Fluxes in the x-direction must exist to compensate the concentration sink existing in the catalytic surface (plane y-z). Solving the closed line integral

$$\langle v_z\rangle_{A_C}\,\frac{d\langle C_{i,j}\rangle_{A_C}(z)}{dz} = \frac{\Delta y}{A_C}\left[N_i(z)\big|_{x_j} + N_i(z)\big|_{x_{j+1}}\right] = a_{v,j}\left[N_i(z)\big|_{x_j} + N_i(z)\big|_{x_{j+1}}\right] \tag{4}$$

Note that the line integral in Δx is zero, because as said before, along the x-coordinate the reactor wall is not permeable. Note also that $\Delta y/A_C = \Delta y\Delta z/A_C\Delta z = \Delta A_{G-S}/\Delta V = a_{v,j}$ is the external, catalytic surface area per unit volume for each j-region. When there is kinetic control, the mass fluxes toward the catalytic surfaces must be equal to the heterogeneous reaction rate

$$\langle v_z\rangle_{A_C}\,\frac{d\langle C_{i,j}\rangle_{A_C}(z)}{dz} = a_{v,j}\left[R^{\text{Het}}_{i,j}(z)\big|_{x_j} + R^{\text{Het}}_{i,j}(z)\big|_{x_{j+1}}\right] \tag{5}$$

Equation 5 must be solved with the boundary condition

$$z = 0 \quad \langle C_{i,j}\rangle_{A_C} = C^0_{i,j} \tag{6}$$

Kinetic Model

In Eq. 5 a reaction kinetics expression is needed. It is convenient to support the kinetic model with a reaction sequence. We propose one, derived from the well-known catalyst activation mechanism, and the atomic chlorine chain reaction degradation sequence previously reported.[13,14] It is described in Table 1. One can work with the first six reactions. Writing the reaction rates for electrons, holes and hydroxyl radicals and applying the local reaction equilibrium approximation (LREA), well-known as the micro steady-state approximation in the unsteady-state reactors for highly reactive intermediates, the concentration of hydroxyl radicals is found to be

$$[\text{OH}\bullet] = \frac{k_1k_2}{2k_4k_5}\,\frac{[\text{OH}^-]_{\text{ad}}[\text{Ti}^{+4}]}{[\text{TCE}]_{\text{ad}}} \times \left(-1 + \sqrt{1 + \frac{4k_4}{k_1k_2[\text{OH}^-]_{\text{ad}}[\text{Ti}^{+4}]}\,R^*_g}\right) \tag{7}$$

R^*_g is the superficial rate of electrons and holes generation. The brackets stand for concentrations, and the subscript ad denotes adsorption. Similarly, one can write the reaction rates for atomic chlorine, and radicals $R_1\bullet$, $R_2\bullet$, $R_3\bullet$ and $R_4\bullet$ (using reactions 6 to 13 in Table 1) and apply again the LREA to obtain the atomic chlorine concentration

$$[\text{Cl}\bullet] = \frac{k_5}{k_{12}[\text{M}]_{\text{ad}}}\,[\text{TCE}]_{\text{ad}}[\text{OH}\bullet]_{\text{ad}} \tag{8}$$

The TCE degradation reaction is produced in two parallel steps

$$R_{\text{TCE}} = \underbrace{-k_5[\text{TCE}]_{\text{ad}}[\text{OH}\bullet]_{\text{ad}}}_{\text{Molecular reaction attack by OH}\cdot} - \underbrace{\text{k}_6[\text{TCE}]_{\text{ad}}[\text{Cl}\cdot]_{\text{ad}}}_{\text{Chain reaction attack involving Cl}\cdot} \tag{9}$$

R_{TCE} corresponds, in this case, to the heterogeneous reaction in Eq. 5. The kinetic expression derived from Eq. 9 must be substituted into Eq. 5.

Using Eqs. 7 and 8

$$R_{\text{TCE}} = -\left(\frac{k_1k_2}{2k_4} + \frac{k_1k_2k_6}{2k_4k_{12}[M]_{\text{ad}}}\,[\text{TCE}]_{\text{ad}}\right)[\text{OH}^-]_{\text{ad}}[\text{Ti}^{+4}] \times \left(-1 + \sqrt{1 + \frac{4k_4R^*_g}{k_1k_2[\text{OH}^-]_{\text{ad}}[\text{Ti}^{+4}]}}\right) \tag{10}$$

The chain reactions occurring on the surface of the catalyst are considered to be responsible for the higher reaction rates observed in the TCE photocatalytic oxidation.[13,14] Hence, the contribution to the overall rate of TCE is greater due to the chlorine atom attack than to the hydroxyl radical attack only. This is consistent with the fact that the rates for nonchlorinated species are lower than the rates for TCE under identical conditions.[20] Then, we obtain

$$R_{\text{TCE}} = -\left(\frac{k_1k_2k_6[\text{OH}^-]_{\text{ad}}[\text{Ti}^{+4}]}{2k_4k_{12}[M]_{\text{ad}}}\,[\text{TCE}]_{\text{ad}}\right) \times \left(-1 + \sqrt{1 + \frac{4k_4R^*_g}{k_1k_2[\text{OH}^-]_{\text{ad}}[\text{Ti}^{+4}]}}\right) \tag{11}$$

Table 1. Reaction Sequence for TCE Photocatalytic Degradation in the Gas Phase

TiO_2	$+ h\nu$	$\xrightarrow{\phi}$	h^+	$+ e^-$	$R_g^*(*)$
OH^-	$+ h^+$	$\xrightarrow{k_1}$	OH•		
Ti^{+4}	$+ e^-$	$\xrightarrow{k_2}$	Ti^{+3}		
Ti^{+3}	$+ O_2$	$\xrightarrow{k_3}$	$Ti^{+4} + O_2^-$		
h^+	$+ e^-$	$\xrightarrow{k_4}$	heat		
CCl_2CClH (TCE)	+ OH•	$\xrightarrow{k_5}$	CCl_2CHOH	+ Cl•	
CCl_2CClH	+ Cl•	$\xrightarrow{k_6}$	$CHCl_2CClCl•$ (R_1•)		
$CHCl_2CClCl•$	$+ O_2$	$\xrightarrow{k_7}$	$CHCl_2CCl_2OO•$ (R_2•)		
$2CHCl_2CCl_2OO•$		$\xrightarrow{k_8}$	$2CHCl_2CCl_2O•$ (R_3•)	$+ O_2$	
$CHCl_2CCl_2O•$		$\xrightarrow{k_9}$	$CHCl_2COCl$ (P_1)	+ Cl•	
$CHCl_2CCl_2O•$		$\xrightarrow{k_{10}}$	$CHCl_2•$ (R_4•)	$+COCl_2$ (P_2)	
$CHCl_2•$	$+ O_2$	$\xrightarrow{k_{11}}$	CO_2	+ HCl	+ Cl•
Cl•	$+ M$	$\xrightarrow{k_{12}}$	M	+ HCl	(**)

Note: In this table all chemical species are adsorbed on the catalytic surface.
(*)R_g^*: superficial rate of electron-hole generation.
(*)(*)Suggested as a possible termination reaction when water is present in the system.[19]

The adsorbed concentration of TCE can be obtained from a balance of sites, according to the reaction sequence described in Table 2

$$[\mathrm{TCE}]_{ad} = [S]_{\mathrm{Total}} \frac{K_{\mathrm{TCE}}[\mathrm{TCE}]}{1 + K_{\mathrm{TCE}}[\mathrm{TCE}] + K_w[\mathrm{H_2O}] + \sum_{i=1}^{i=N} K_i[P_i]} \tag{12}$$

The concentration of reaction intermediates is undetectable as it will be shown later. In addition to this, it must be considered that under our experimental conditions the ratio $[H_2O]/[TCE]$ varies from a minimum value of 2.3×10^3 to a maximum of 10.2×10^3. Therefore, compared with the other terms, it seems feasible to neglect $\sum_{i=1}^{N} K_i[P_i]$ in Eq. 12.

Table 2. Reaction Sequence for a Balance of Active Sites in TCE Degradation

S	+	TCE	$\rightleftarrows^{K_{\mathrm{TCE}}}$	TCE(ad)
S	+	H_2O	$\rightleftarrows^{K_w}$	H_2O(ad)
S	+	P_i	$\rightleftarrows^{K_{P_i}}$	P_i(ad)

S: active site for adsorption
P_i: reaction products

Defining the following apparent constants

$$\alpha_1^* = \frac{k_1 k_2 k_6 [\mathrm{OH^-}]_{ad}[\mathrm{Ti^{+4}}]}{2k_4 k_{12}[M]_{ad}} \quad \text{and} \quad \alpha_2^* = \frac{4k_4}{k_1 k_2 [\mathrm{OH^-}]_{ad}[\mathrm{Ti^{+4}}]} \tag{13}$$

and considering that $\alpha_1 = \alpha_1^*[S]_{\mathrm{Total}}$, the rate of TCE degradation becomes

$$R_{\mathrm{TCE}} = -\alpha_1 \frac{K_{\mathrm{TCE}}[\mathrm{TCE}]}{1 + K_{\mathrm{TCE}}[\mathrm{TCE}] + K_w[\mathrm{H_2O}]} (-1 + \sqrt{1 + \alpha_2^* R_g^*}) \tag{14}$$

When $\alpha_2^* R_g^* \ll 1$, the following substitution applies: $\sqrt{1 + \alpha_2^* R_g^*} \cong 1 + (1/2)\alpha_2^* R_g^*$. Then, when the rate of electron-hole generation is low, the following reaction rate is obtained

$$R_{\mathrm{TCE}} = -\alpha_3 \frac{K_{\mathrm{TCE}}[\mathrm{TCE}]}{1 + K_{\mathrm{TCE}}[\mathrm{TCE}] + K_w[\mathrm{H_2O}]} R_g^* \tag{15}$$

In Eq. 15 $\alpha_3 = \alpha_1(\alpha_2^*/2)$.

When $\alpha_2^* R_g^* \gg 1$, Eq. 14 yields

$$R_{\mathrm{TCE}} = -\alpha_4 \frac{K_{\mathrm{TCE}}[\mathrm{TCE}]}{1 + K_{\mathrm{TCE}}[\mathrm{TCE}] + K_w[\mathrm{H_2O}]} \sqrt{R_g^*} \qquad (16)$$

In Eq. 16 $\alpha_4 = \alpha_1\sqrt{\alpha_2^*}$.

The rate of electron-hole generation (the catalyst activation reaction, Eq. 1 in Table 1) must be directly proportional to the absorbed light intensity, the proportionality constant being the primary quantum yield. Thus, in Eq. 14 the two known possibilities in photocatalytic reactions can be found: (1) For $\alpha_2^* R_g^* \gg 1$ the square root dependence with the rate of photon absorption will be observed (Eq. 16), and (2) when $\alpha_2^* R_g^* \ll 1$ the linear dependence will prevail (Eq. 15). Moreover, there may be a region where both kinetic regimes coexist, and Eq. 14 should be used. The switch from one regime to the other depends on the relative values of the absorbed intensities in relation to the following ratio of kinetic constants: $k_4 / k_1 k_2$. Interesting to note, this ratio is the relationship between the rate constants of the recombination reaction, and the product of those corresponding to the combination reactions of both charge carriers.

As indicated earlier, through the value of R_g^* in Eq. 14 it is clear that the reaction rate depends on the light intensity. The field of radiation intensities has to be known before the specific relationship between the intensity at a given point, and the kinetic effect of the absorption of this energy is developed; that is, before the specific discussion of an expression for R_g^* is made.

Radiation Field Inside the Reactor

In a previous work, the radiation field corresponding to the employed reactor was studied but using different catalytic meshes.[9] The model describes the existing field in the space between catalytic surfaces on the assumption that the interjacent medium does not influence radiation transport; that is, the only elements that affect the radiation distribution are the titanium dioxide coated meshes, because the fluid existing between the stiff grids does not participate in the radiation exchange. These flat surfaces, arranged as a series of parallel planes, produce diffuse transmission and reflection, as well as absorption on those parts covered by the solid semiconductor. On these grounds a one-dimensional, diffuse-transmission-reflection model was presented for catalytic planes numbered generically with the index j. The space j is located between mesh j and mesh j + 1. It was shown that in each generic region j the specific intensity is

$$I_j(x, y, z, \underline{\Omega}) = I_j^+(x, y, z, \underline{\Omega}) H(\underline{\Omega} \cdot \underline{e}_x) + I_j^-(x, y, z, \underline{\Omega}) H(-\underline{\Omega} \cdot \underline{e}_x) \quad j = 0, 1, \ldots, N \qquad (17)$$

H is the step function, I_j^+ and I_j^- indicate intensities in the forward (+x) direction and backward (-x) direction, respectively. Similarly, it was deduced that the incident radiation is represented by

$$G_j(x, y, z) = \int_{4\pi} I_j(x, y, z, \underline{\Omega})\, d\Omega = G_j^+(x, y, z) + G_j^-(x, y, z) \quad j = 0, 1, \ldots, N \qquad (18)$$

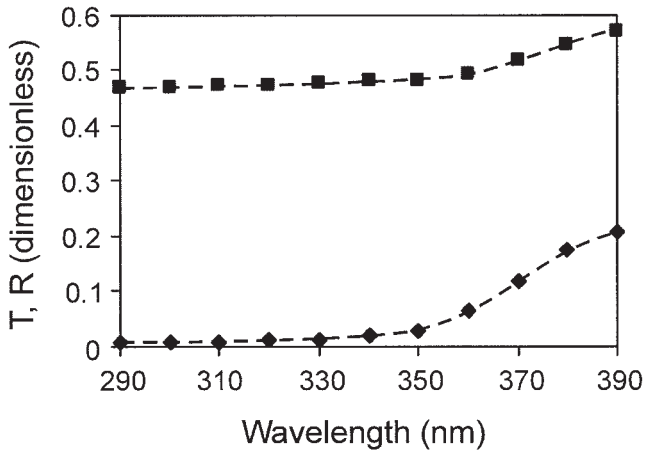

Figure 4. Experimental values of the transmittance (■), and reflectance (♦) of the catalytic meshes.

Furthermore, it was shown that for this arrangement

$$G_j = 2\pi(I_j^+ + I_j^-) \qquad (19)$$

Applying an adaptation of the ray-tracing technique,[21] and considering reflection and transmission by the windows and the coated fiber meshes, the following final results for radiation intensities with bilateral irradiation were obtained

$$I_j^+ = I_0^+ \frac{T_{j+W} + T_{N-j+W} R_{j+W}}{1 - R_{N-j+W} R_{j+W}} \qquad (20)$$

$$I_j^- = I_0^+ \frac{T_{j+W} R_{N-j+W} + T_{N-j+W}}{1 - R_{N-j+W} R_{j+W}} \qquad (21)$$

with

$$T_N = \frac{T_{N-1} T_1}{1 - R_{N-1} - R_1} \quad \text{and} \quad R_N = R_1 + \frac{T_1^2 R_{N-1}}{1 - R_1 R_{N-1}} \qquad (22)$$

and, the following relationships hold

$$I_j^+ = I_{N-j}^- \quad \text{and} \quad I_j^- = I_{N-j}^+ \qquad G_j = G_{N-j} \qquad (23)$$

As indicated before, values of the reflection and transmission properties of the acrylic windows (W) have been previously published. For the new catalytic meshes the corresponding R and T values are needed. The employed experimental procedure reproduced the methodology described in details before[9] and will not be repeated here. Figure 4 shows the experimental results. It is important to note that the newly adopted meshes are very different than the ones used before (compare Figure 4 in this work with Figure 6b in the quoted reference). The reflectance is lower and transmittance is significantly higher, the main reason being that the commercial glass fiber that served as a support for the catalyst in this work consisted in a coarser fabric. This characteristic of the catalytic plates trans-

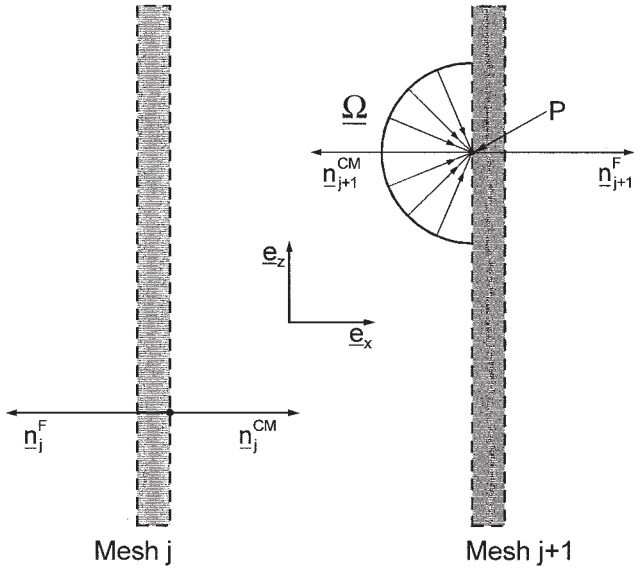

Figure 5. Model for calculating R^*_g.

lates into less abrupt transitions in the radiation field when moving between adjacent meshes.

Activation Step

In this section the following question is answered: What is the rate of generation of electrons and holes resulting from catalyst activation by the presence of the radiation field given by Eqs. 17 to 23?

Consider one point on the solid part of the glass fiber mesh coated with titanium dioxide. This point is on the mesh j+1 and is irradiated by the existing radiation field between mesh j and mesh j+1 (Figure 5). This point is characterized by a position vector

$$\underline{r}_P = \underbrace{x_{j+1}e_x}_{\substack{x\text{-position of mesh } j+1 \text{ coated} \\ \textit{with titanium dioxide}}} + \underbrace{y^{CM}_{j+1}e_y + z^{CM}_{j+1}e_z}_{\substack{y \text{ and } z \text{ position on the surface} \\ \text{of } TiO_2 \text{ coated mesh } j+1}} \quad (24)$$

The outwardly directed unit normal vector to the coated mesh is $\underline{n}^{CM}_{j+1}$, and the equivalent normal to the fluid is $\underline{n}^{F}_{j+1} = -\underline{n}^{CM}_{j+1}$. Only those directions having $\underline{\Omega} \cdot \underline{n}^{F}_{j+1} > 0$ can be absorbed. The rate of electron-hole generation can be written in terms of the absorbed radiation and a primary quantum yield for the activation step. For monochromatic radiation between λ and $\lambda + d\lambda$ and a differential catalytic surface area dA^{22}_{CM}

$$dR_{g,\lambda}(x_{j+1}, y^{CM}_{j+1}, z^{CM}_{j+1}) = \phi_\lambda \left[\int_{4\pi} I_{j,\lambda}(x_{j+1}, y^{CM}_{j+1}, z^{CM}_{j+1}, \underline{\Omega}) H(\underline{\Omega} \cdot \underline{n}^{F}_{j+1}) \underline{\Omega} \cdot \underline{n}^{F}_{j+1} \, d\Omega \right] dA_{CM} \quad (25)$$

In Eq. 25 $I_{j,\lambda}$ is the existing monochromatic intensity in the gap j between mesh j and mesh $j+1$, and the step function H selects the rays that are absorbed.

It can be noted that $\underline{n}^{F}_{j+1} = \underline{e}_x$ and $H(\underline{\Omega} \cdot \underline{n}^{F}_{j+1}) H(-\underline{\Omega} \cdot \underline{e}_x) = 0$. Then, substituting Eq. 17 into Eq. 25

$$dR_{g,\lambda}(x_{j+1}, y^{CM}_{j+1}, z^{CM}_{j+1}) = \phi_\lambda \left[\int_{4\pi} I^{+}_{j,\lambda}(x_{j+1}, y^{CM}_{j+1}, z^{CM}_{j+1}, \underline{\Omega}) H(\underline{\Omega} \cdot \underline{n}^{F}_{j+1}) \underline{\Omega} \cdot \underline{n}^{F}_{j+1} \, d\Omega \right] dA_{CM} \quad (26)$$

In the coated meshes it is possible to assume that transmission and reflection is diffuse (cf. previously described model), that is, intensities are not a function of direction. Then

$$dR_{g,\lambda}(x_{j+1}, y^{CM}_{j+1}, z^{CM}_{j+1}) = \phi_\lambda I^{+}_{j,\lambda}(x_{j+1}, y^{CM}_{j+1}, z^{CM}_{j+1}) \times \left[\int_{4\pi} H(\underline{\Omega} \cdot \underline{n}^{F}_{j+1}) \underline{\Omega} \cdot \underline{n}^{F}_{j+1} \, d\Omega \right] dA_{CM} \quad (27)$$

The integral in Eq. 27 can be immediately evaluated because considering spherical coordinates $\underline{\Omega} \cdot \underline{n}^{F}_{j+1} = \cos\theta$ and $d\Omega = \sin\theta \, d\theta \, d\varphi$. The step function defines the half space for which $\underline{\Omega} \cdot \underline{n}^{F}_{j+1} > 0$. After integration

$$\int_{4\pi} H(\underline{\Omega} \cdot \underline{n}^{F}_{j+1}) \underline{\Omega} \cdot \underline{n}^{F}_{j+1} \, d\Omega = 2\pi \left(\frac{\sin^2\theta}{2} \Big|_0^{\pi/2} \right) = \pi \quad (28)$$

Hence

$$dR_{g,\lambda}(x_{j+1}, y^{CM}_{j+1}, z^{CM}_{j+1}) = \pi \phi_\lambda I^{+}_{j,\lambda}(x_{j+1}, y^{CM}_{j+1}, z^{CM}_{j+1}) dA_{CM} \quad (29)$$

It can be noted that the coated surface area A_{CM} can be written in terms of the total mesh surface area and the fraction of solid coated mesh as follows: $dA_{CM} = \varepsilon_{CM} dA_M$. Integrating over the whole surface and the whole interval of wavelengths of interest

$$R_{g,j+1} = \varepsilon_{CM} \pi \int_{\lambda_1}^{\lambda_2} \phi_\lambda \iint_{A_M} I^{+}_{j,\lambda}(x_{j+1}, y_{j+1}, z_{j+1}) dA_M d\lambda \quad (30)$$

In a previous work[9] it was shown that the radiation field on the space between meshes at each different position (1, . . ., N) is fairly uniform in the y and z directions. Then, an average value of the intensity can be defined over A_M. Furthermore, from Eq. 19: $I^{+}_{j,\lambda} = G^{+}_{j,\lambda}/2\pi$, then

$$R_{g,j+1} = \frac{1}{2} A_M \varepsilon_{CM} \int_{\lambda_1}^{\lambda_2} \phi_\lambda \langle G^{+}_{j,\lambda} \rangle_{A_M} \, d\lambda \quad (31)$$

$$R_{g,j} = \frac{1}{2} A_M \varepsilon_{CM} \int_{\lambda_1}^{\lambda_2} \phi_\lambda \langle G^{-}_{j,\lambda} \rangle_{A_M} \, d\lambda \quad (32)$$

The superficial rate of electron-hole generation (moles s^{-1} m^{-2}) is finally

$$R^*_{g,j+1} = \frac{1}{2}\,\varepsilon_{CM}\int_{\lambda_1}^{\lambda_2}\phi_\lambda\langle G^+_{j,\lambda}\rangle_{A_M}\,d\lambda \tag{33}$$

In a similar way

$$R^*_{g,j} = \frac{1}{2}\,\varepsilon_{CM}\int_{\lambda_1}^{\lambda_2}\phi_\lambda\langle G^-_{j,\lambda}\rangle_{A_M}\,d\lambda \tag{34}$$

Defining

$$\langle G_j\rangle_{A_M} = \int_{\lambda_1}^{\lambda_2}\langle G_{j,\lambda}\rangle_{A_M}\,d\lambda \quad \text{and} \quad \bar{\phi} = \frac{\int_{\lambda_1}^{\lambda_2}\phi_\lambda\langle G_{j,\lambda}\rangle_{A_M}d\lambda}{\int_{\lambda_1}^{\lambda_2}\langle G_{j,\lambda}\rangle_{A_M}\,d\lambda} \tag{35}$$

$$R^*_{g,j+1} = \frac{1}{2}\,\varepsilon_{CM}\bar{\phi}\langle G^+_j\rangle_{A_M} \tag{36}$$

and

$$R^*_{g,j} = \frac{1}{2}\,\varepsilon_{CM}\bar{\phi}\langle G^-_j\rangle_{A_M} \tag{37}$$

The values of the incident radiation (G_j^+ and G_j^-) can be obtained from Eqs. 19 to 23. The total rate of electron-hole generation in each section j results equal to

$$R^T_{g,j} = \frac{1}{2}\,\varepsilon_{CM}\bar{\phi}[\langle G^+_j\rangle_{A_M} + \langle G^-_j\rangle_{A_M}] = \frac{1}{2}\,\varepsilon_{CM}\bar{\phi}\langle G^T_j\rangle_{A_M} \tag{38}$$

Final Reactor and Reaction Kinetic Model

Combining Eqs. 5, 14 and 38, the reactor-reaction model for the photo-oxidation of TCE in the j-region is obtained

$$v_z\left.\frac{d[\mathrm{TCE}]}{dz}\right|_j = -\alpha_1 a_{v,j}\left(\frac{K_{\mathrm{TCE}}[\mathrm{TCE}]}{1 + K_{\mathrm{TCE}}[\mathrm{TCE}] + K_w[\mathrm{H_2O}]}\right)\Bigg|_j \times (-1 + \sqrt{1 + \alpha_2\varepsilon_{CM}\langle G^T_j\rangle_{A_M}}) \tag{39}$$

where $\alpha_2 = \alpha_2^*(1/2)\bar{\phi}$. In order to simplify the notation a change has been introduced in Eq. 39. It must be understood that, in this equation, concentrations written between brackets correspond in effect to velocity weighted, cross-section averaged concentrations. Equation 39 can be integrated to give

$$[\mathrm{TCE}]^{\mathrm{exit}}_j = [\mathrm{TCE}]_0 \times \exp\left\{-\frac{K_{\mathrm{TCE}}}{1 + K_w[\mathrm{H_2O}]}\left[\frac{\alpha_1 a_{v,j}L}{v_z}(-1 + \sqrt{1 + \alpha_2\varepsilon_{CM}\langle G^T_j\rangle_{A_M}}) + [\mathrm{TCE}]^{\mathrm{exit}}_j - [\mathrm{TCE}]_0\right]\right\} \tag{40}$$

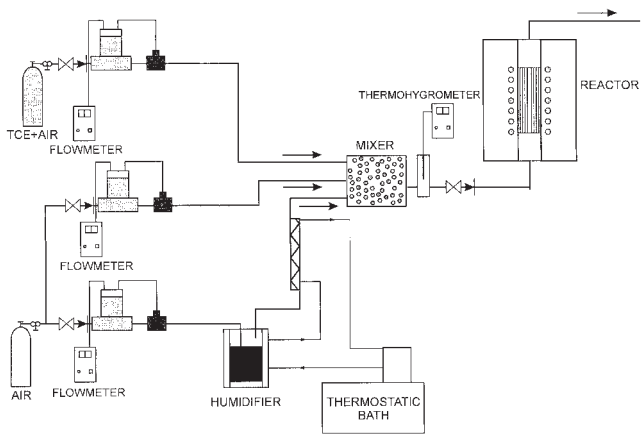

Figure 6. Experimental setup.

This equation can be solved iteratively. The result for the reaction space j must be extended to the observed changes in the whole reactor (all meshes). We have also that

$$\sum_{j=0}^{j=N} Q_j[\mathrm{TCE}]^{\mathrm{exit}}_j = Q[\mathrm{TCE}]^{\mathrm{exit}}_{\Sigma j} \tag{41}$$

Finally

$$[\mathrm{TCE}]^{\mathrm{exit}}_{\Sigma j} = \sum_{j=0}^{j=N}\frac{Q_j}{Q}[\mathrm{TCE}]^{\mathrm{exit}}_j = \sum_{j=0}^{j=N}\frac{A_{C,j}}{A_{C,T}}[\mathrm{TCE}]^{\mathrm{exit}}_j \tag{42}$$

$[\mathrm{TCE}]^{\mathrm{exit}}_{\Sigma j}$ is the theoretical exit concentration that must be compared with the experimental results.

Experiments

The reacting system was fed with three different streams (Figure 6). Two of them provided air (gas chromatographic quality, from Air Liquide), and the third one furnished a mixture of air of the same quality and a known concentration of TCE. This mixture was specially prepared from liquid TCE (Merck) and air, and the resulting concentration was measured by gas chromatography. One of the two pure air streams was saturated with water vapor by bubbling in distilled water (a humidifier) operated at constant temperature (20°C). The flow rates of the three gaseous streams were regulated with mass flow controllers on line (Matheson Corp.). The three streams were mixed in the desired proportions, and the resulting vapor concentration and temperature were measured with a thermo-hygrometer (Oakton Corp.). The mixed stream passed through a sampling port and afterwards was fed to the reactor. The exit line from the reactor had provision for gaseous sampling and the exiting gas was safely disposed in a gas scrubber. Samples were analyzed by gas chromatography (Hewlett Packard 5890). In this way four variables were precisely controlled: temperature, total flow rate, TCE concentration and water vapor concentration.

The illuminating system (seven lamps placed in a box at each side of the reactor) permitted to interpose between the

lamps and the reactor windows specially constructed filters to modify and control the radiation fluxes reaching the catalytic meshes. These filters were constructed on red sensitive films (polyester base, thickness = 0.1 mm) for recorders with He-Ne laser (HNm from AGFA Alliance Recording) from patterns made with different gray tonalities produced with the aid of a Corel Draw software. The optical and mechanical stability of these films were verified with exposures to the employed light for over 15 h; no measurable changes in their characteristics were observed. This control was made by measuring the transmittance of the films as a function of wavelength in a PerkinElmer (Lambda 40) spectrophotometer. The wavelength distributions of the lamp output (dotted lines), and those corresponding to the transmission of the employed filters (solid lines), are shown in Figure 7. The percent transmittance of each filter is defined as

$$T = \frac{\int_{\lambda_1}^{\lambda_2} G_\lambda T_\lambda d\lambda}{\int_{\lambda_1}^{\lambda_2} G_\lambda d\lambda} \tag{43}$$

This procedure allowed a controlled variation of a fifth experimental parameter: the arriving light intensities to the reactor windows.

For the set of runs carried out under the kinetic control regime and at constant irradiating conditions, a metallic mesh, acting as a screen and having a 7.8% transmission, was interposed between the lamps and each of the reactor windows.

A typical run lasted for 5 h, allowing for sufficient time to reach steady-state operation of flow rates, concentrations and temperatures. Under steady-state operation, the presence of reaction intermediates was undetectable within the detection limits of GCMS measurements (Shimadzu QP5000). Thus, for the kinetic study, besides water vapor, TCE was the only significant component detected in the reactor feed and outlet streams.

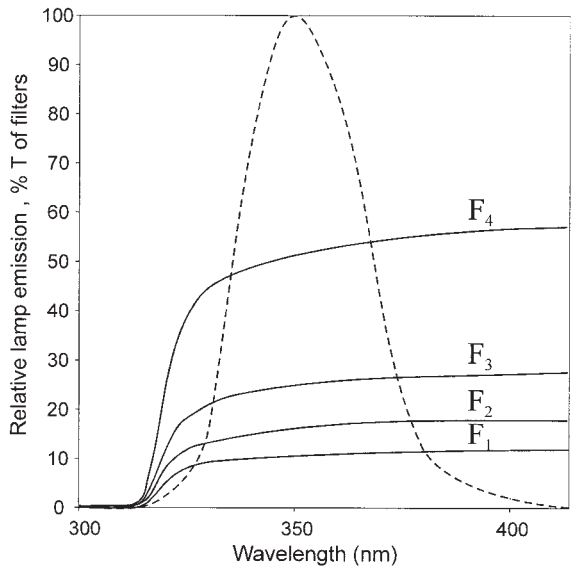

Figure 7. Distribution of the lamp output power (broken line); % transmission of the filters, both as a function of wavelength.

Table 3. Typical Reactor Performance

Q (cm^3 min^{-1})	X_{TCE} C^0_{TCE} = 27 mg m^{-3}	X_{TCE} C^0_{TCE} = 42 mg m^{-3}
100	0.87	0.92
500	0.81	0.84
1000	0.72	0.77
1500	0.42	0.53

However, in order to verify the consistency of the proposed kinetic model, experiments were conducted employing very high initial TCE concentrations. Values as high as 800 mg/m^3 (30 times higher than the concentrations employed in the kinetic study) were used. Under these conditions very small GCMS peaks corresponding to phosgene and DCAC were detected. These two reaction intermediates are included in the reaction scheme shown in Table 1.

Preliminary Results

Table 3 shows the results of the experimental conversion of TCE at the reactor outlet. For these runs the reactor was operated with four meshes, bilateral irradiation, two different concentrations in the feed and increasing flow rates. It can be observed that the efficiency of this fixed-bed reactor (the total surface area of the employed meshes was 0.1368 m^2) is very high, achieving conversions above 90%. Even for rather high flow rates (1,500 cm^{3}min^{-1}) conversions are always higher than 40%. Increasing flow rate the conversion decreases due to the corresponding decrease in the average residence time.

To obtain meaningful kinetic parameters it is necessary to confirm that the reactor operation is made under conditions of a kinetic control regime. Performing an integral mass balance in the reactor it is possible to define a global reaction rate that corresponds to the average reaction rate over the total active surface area of all meshes

$$\langle R_{TCE} \rangle_{A_{total}} = \frac{X_{TCE}\, Q\, C^0_{TCE}}{N\, \varepsilon_{CM}\, A_M} \tag{44}$$

In Eq. 44, N is the number of meshes, A_M is the area of each mesh, X_{TCE} is the TCE exit conversion, Q is the total flow rate entering the reactor, ε_{CE} is the fraction corresponding to the solid area of each mesh, and C^0_{TCE} is the feed concentration of TCE. Under kinetic control regime, for a fixed reactor configuration, constant illumination and constant TCE feed concentration, the product of the volumetric flow rate times the conversion should be constant; that is, the reaction rate cannot change with the flow rate. If this is not the case, and the rate increases with flow rate, the reactor has an operation partially or totally controlled by mass transport. It was observed that all the typical runs shown in Table 3 did not correspond to data in the kinetic control regime. In order to solve this problem and be able to obtain meaningful kinetic constants the operating conditions had to be changed. For this purpose the irradiation rate was reduced to 7.8% of the one corresponding to the initial design and the flow rate was further increased beyond 1,500 cm^{3}min^{-1}. This procedure was done for different feed concentrations (of both TCE and humidity) until the reaction rate became independent of the flow rate. Figure 8 a and b shows these effects for two different inlet concentrations of TCE and

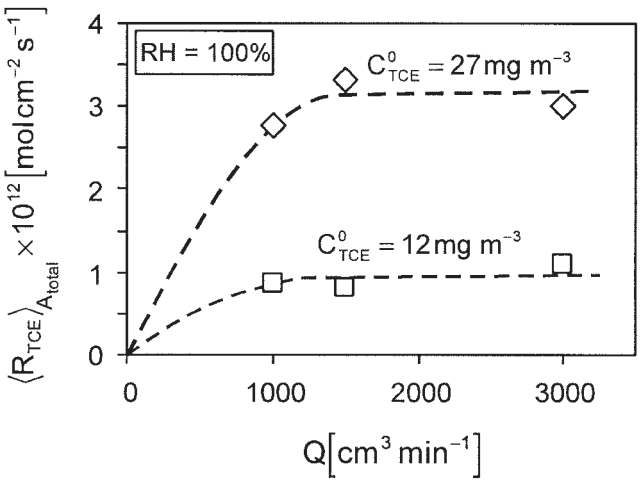

(a)

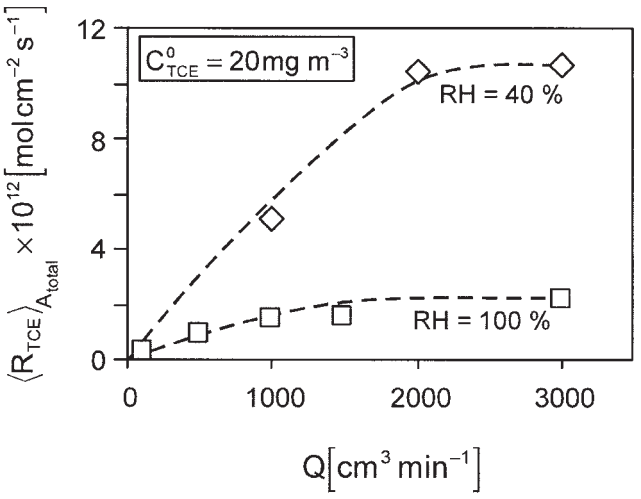

(b)

Figure 8. Operating regions of the kinetic control regime. (a) C^0_{TCE} is the parameter, and (b) relative humidity is the parameter.

two different water vapor concentrations. Two clearly distinct zones can be observed: (1) low flow rates, where diffusion is controlling the rates, and (2) high flow rates (above 2,900 $cm^3 min^{-1}$), where the chemical reaction on the surface of the meshes is the controlling step. In the first zone, increasing flow rates the mass transfer rates are improved and the global reaction rate also increases. In the second zone, when the mass transfer control becomes negligible, the reaction rate does not change any longer, providing the region where the parameter estimation can be performed. It must be noted that the stated flow rate and irradiation rate where the kinetic regime prevails, corresponds to a range of humidity above 40%. Below this value and for the achievable flow rates in the available reactor set up, mass transfer control was always present.

Results Under Kinetic Control Regime

Figure 9 shows results obtained under relative humidity of 100%, employing the neutral mechanical screen with a 7.8% light transmission, and a flow rate of 3,000 $cm^3\ min^{-1}$ allowing for changes in the initial TCE concentration. These results show a behavior very close to a typical first-order dependence, indicating that very likely, $K_{TCE} \times$ [TCE] in Eq. 14 is very small.

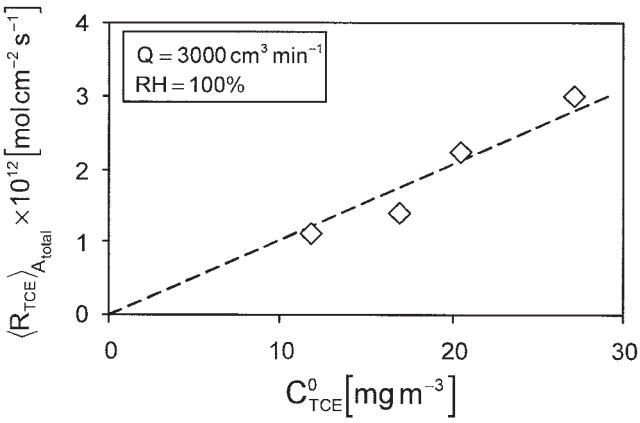

Figure 9. Effect of TCE concentration on the reaction rate.

Figure 10 shows the results of varying the relative humidity in the range of 40% $<$ RH $\leq$ 100%, using the same neutral mechanical screen. It can be observed a pronounced effect of the water vapor concentration on the average rate. Changing the relative humidity from 40 to 100%, the average rate is decreased by one order of magnitude. This is the result of a competitive effect of the water molecules for the active sites of the catalyst, a typical result previously reported by Dibble and Raupp,[10] Raupp et al.,[2] Wang et al.,[12] Amama et al.,[13] and Zhao et al.[14] This behavior should be taken into account for the kinetic model developed in Eq. 14.

Overall quantum yields depend on many operation conditions, for example, the relative humidity, the initial TCE concentration, the activity of the catalytic surface and the range of irradiation rates. They can be determined using data obtained with the mechanical screen under kinetic control regime. The following values result

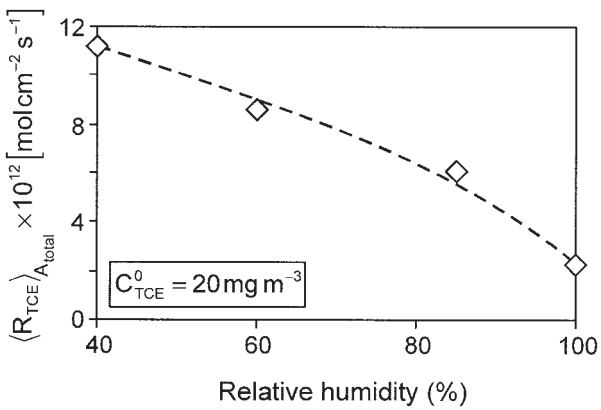

Figure 10. Effect of relative humidity on the reaction rate.

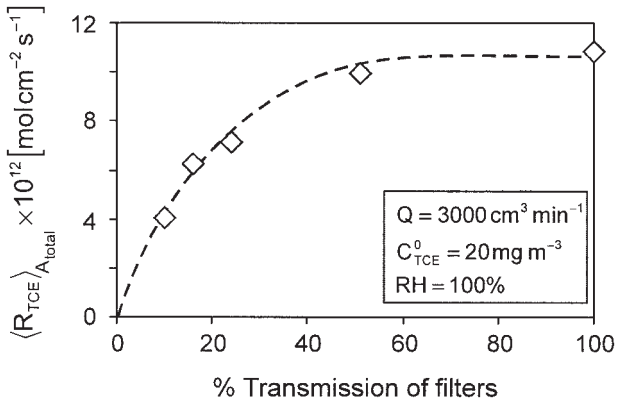

Figure 11. Effect of the incident radiation on the reaction rate.

Relative Humidity (%)	Quantum Yield (%)
40	5.60
60	4.30
85	3.05
100	1.10

It can be noted that quantum yields decrease when the relative humidity is increased, a result that is consistent with the proposed competitive adsorption effect of water vapor with TCE for the catalyst active sites and the inhibition of the Cl-atom promoted chain reaction proposed in the adopted reaction scheme.

Employing the set of filters described above, a second group of runs were performed varying the existing radiation field in the space where the catalytic meshes are placed. These runs were performed at flow rate (Q = 3,000 cm^{3}min^{-1}), initial *TCE* concentration (C^0_{TCE} = 20 mg m^{-3}) and relative humidity (RH = 100%) constant. The irradiation boundary condition to each of the reactor windows was changed employing filters F_1, F_2, F_3, and F_4, as well as no filters (100% irradiation). Figure 11 shows the results. Clearly, when irradiation was produced with an intensity corresponding to a transmission above 25% of that of the initial design, the reaction became mass transfer limited, a phenomenon that is dramatically significant for transmissions beyond 50%. Thus, as indicated by the theory, at sufficiently high irradiation rates, the rate shows zero-order dependence with respect to the absorbed light intensity, indicating that mass transport of TCE to the catalytic surface cannot compensate the reactant consumption derived from the existence of a very large amount of available photons. Hence, the only runs that are useful for estimating the kinetic parameters are those carried out with filters F_1, F_2 and F_3, and the mechanical screens. Estimating the reaction order for the light intensity dependence (actually for the incident radiation dependence according to Eqs. 33 and 34) from the results of these runs, one should be able to decide if kinetic Eq. 15 or 16 applies for this case, or it is necessary to consider an intermediate case as shown by Eq. 14.

Parameter's Estimation

For estimating the reaction parameters, a computed code was used which solves a nonlinear least-square problem, using a modified Levenberg-Marquardt algorithm. The product of $K_W[H_2O]$ is large compared with the other terms in the denominator of Eq. 39. This is in accordance with the almost first-order behavior observed in Figure 9. As a consequence, Eq. 40 yields

$$[\mathrm{TCE}]_j^{\mathrm{exit}} = [\mathrm{TCE}]_0 \exp\left[-\frac{\alpha_1 K_{\mathrm{TCE}}}{K_w[\mathrm{H_2O}]} \frac{a_{v,j} L}{v_z} \left(-1 + \sqrt{1 + \alpha_2 \varepsilon_{\mathrm{CM}} \langle G_j^T \rangle_{A_M}}\right)\right] \quad (45)$$

Table 4. Kinetic Parameters

Parameter	Value	95% Confidence Interval	Units
$\alpha_1 K_{TCE}/K_w$	1.230	0.085	mg s^{-1} m^{-2}
α_2	1.354×10^6	0.148×10^6	m^2 s einstein^{-1}

Results of the kinetic parameters $\alpha_1 K_{TCE}/K_w$ and α_2, are shown in Table 4.

Table 5 presents the value of $\alpha_2 \varepsilon_{CM} \langle G_j^T \rangle_{A_M}$ in Eq. 45, under different irradiating conditions and for the different j-positions in the reaction space. The reaction order with respect to $\langle G_j^T \rangle_{A_M}$ is a value closer to 0.5 than to 1. The hypothetical, equivalent reaction order corresponds to approximately 0.6. Thus, under these operating conditions, this reaction order shows an intermediate value, meaning that at slightly higher irradiation rates (increasing further the flow rate to remain under the kinetic control regime), very likely the order will be a definite 0.5.

Figure 12 shows predicted vs. experimental concentrations at the reactor outlet. The solid line corresponds to $C_{TCE}|^{exit}_{\Sigma j\ exp} = C_{TCE}|^{exit}_{\Sigma j\ theo}$. TCE conversion, in the experimental program under kinetic control regime, ranged from 9 to 61%. It should be noted that the maximum observed error is never larger than 21%.

Model Results for each Different Reaction Space

Let us first look at the distribution of radiation inside the reactor. Figure 13a represents the total incident radiation $\langle G_j^T \rangle_{A_M}$ (adding contributions produced by irradiation from both sides of the reactor) inside each reaction space between meshes and between meshes and reactor windows. These results were obtained with the model described by Eqs. 19 to 23. Values have been made dimensionless employing the total incident radiation at the reactor window entrance position. The observed symmetry inside the reactor corresponds to the use of bilateral irradiation. The maximum attenuation is observed in the central reaction space where $\langle G_j^T \rangle_{A_M}$ has a value 42% lower than the one at the entrance.

Figure 13b is a representation of the predicted exit conversions in each of the reactor zones for RH = 100%, and irradiation reduced to 10%. Being a first-order reaction with

Table 5. Product $\alpha_2 \varepsilon_{CM} \langle G_j^T \rangle_{A_M}$ for Different Irradiation Conditions in the *J*-Regions

	j-Region				
T (%)	0	1	2	3	4
24	32	24	18	24	32
16	21	14	11	14	21
10	13	9	8	9	13

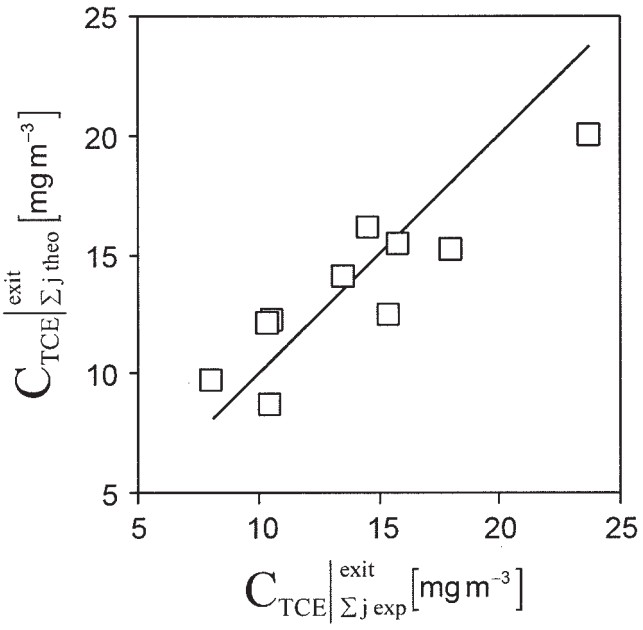

Figure 12. Quality of the radiation and reaction model.

respect to *TCE* concentration, these results are independent of the concentration in the feed and are of general validity for the range in which the kinetic parameters have been estimated. Clearly, the radiation and the conversion profiles in the reactor are symmetric respect to a plane located at the center of the reactor. This result is a consequence of the dependence of the reaction rate with the incident radiation. Notice that regions 0 and 4 are limited by non catalytic, acrylic windows; hence, in these regions there is only one catalytic surface and the *TCE* conversions are lower than those found in the inner regions.

Conclusions

They can be summarized as follows:

- A model has been proposed for the degradation of *TCE* in a wetted air stream, using a fixed-bed photocatalytic reactor. This development uses a radiation field modeled and verified in a previous work.[9]
- The degradation rates of *TCE* with the employed catalytic meshes are very high, turning difficult to find a region of the operating variables where the kinetic control regime is surely established.
- In spite of it, conditions for obtaining data under kinetic control regime have been obtained. Changing irradiation rates (to low values), relative humidity (to values beyond 40%) and flow rates (to the higher permitted values in the available reactor setup) the objective was accomplished.
- Working under these restricted operating conditions the kinetic parameters were estimated.
- The obtained results validated the proposed model. It shows a first-order kinetics with respect to the TCE concentration, a behavior close to a square root dependence with respect to the Incident Radiation and a typical site-competitive kinetics for the dependence with the relative humidity. It must be clearly remarked that the proposed kinetic model has the possibility to represent the full range of potential dependencies with respect to the irradiation rate (reaction orders ranging from 0.5 to 1). In our case, the observed value corresponds to an equivalent order of 0.6, indicating the existence of an intermediate reaction order dependency with respect to the incident radiation.
- It must be noted that the proposed design renders a reasonable uniform irradiation of all the catalytic meshes and a good ratio of the available catalytic surface area with respect to the reaction volume. These two features facilitate to operate with rather high pollutant conversions even in short contact times. In other words, any up-scale of this type of arrangement would be very appropriate for the photocatalytic remediation of polluted air streams.
- Finally, the kinetic model developed under the kinetic control regime, together with the obtained parameters, is the first, unavoidable step toward the development of a complete model for the reactor operating under any practical condition, including the case when mass transport limitations exits.

Acknowledgments

The authors are grateful to the Universidad Nacional del Litoral, the National Research Council of Argentina (CONICET) and the National Agency for Science and Technology of Argentina (ANPCyT) for the financial support. Thanks are also given to Enerzone, Inc., 22 Pleger Street, London, ON, N5Z 2B5, Canada, for furnishing the titanium dioxide coated glass fiber meshes to produce this work. The technical assistance of Eng.

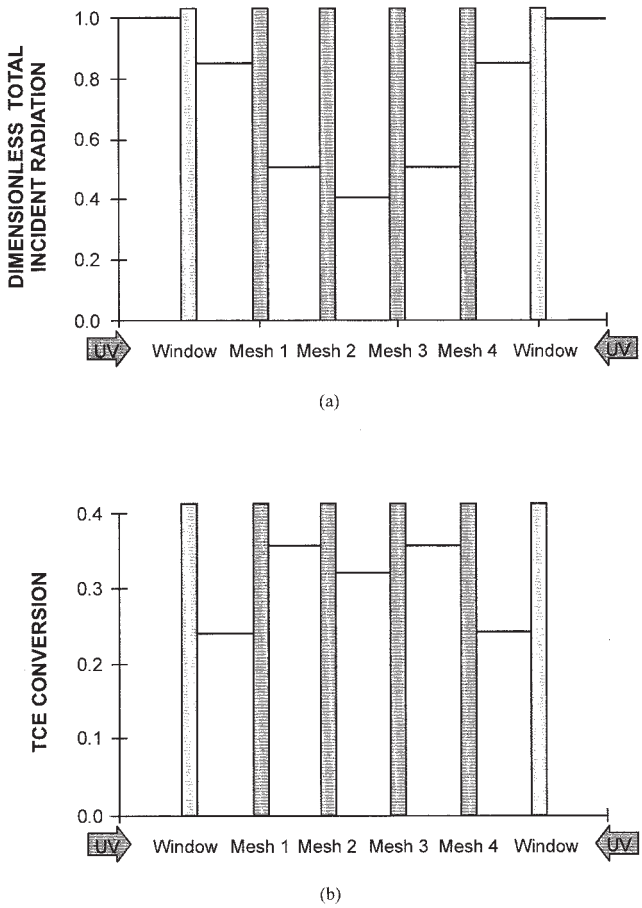

Figure 13. Simulation results. (a) radiation distribution in each region inside the reactor, and (b) TCE conversion in each region inside the reactor.

Claudia Romani is also acknowledged. We also are pleased to recognize useful discussions on the reaction mechanism with Dr. José Peral from the Universidad Autónoma de Barcelona, Spain.

Notation

$A_{c,j}$ = cross-sectional area of j-region, m^2
$A_{c,T}$ = total cross-sectional area, m^2
A_M = area of each mesh, m^2
$C_{i,j}$ = i-species concentration in j-region, mg m^{-3}
$C^0_{i,j}$ = i-species feed concentration in j-region, mg m^{-3}
$\langle C_{i,j}\rangle_{A_C}(z)$ = velocity weighted concentration averaged over the cross sectional area of j-region, mg m^{-3}
I_j = radiation intensity in j-region, Einstein m^{-2} s^{-1} sr^{-1}
I_j^+ = forward radiation intensity in j-region, Einstein m^{-2} s^{-1} sr^{-1}
I_j^- = backward radiation intensity in j-region, einstein m^{-2} s^{-1} sr^{-1}
G_j = total incident radiation in j-region, Einstein m^{-2} s^{-1}
G_j^+ = forward incident radiation in *j*-region, Einstein m^{-2} s^{-1}
G_j^- = backward incident radiation in j-region, Einstein m^{-2} s^{-1}
$\langle G_j^+\rangle_{A_M}$ = forward incident radiation in j-region averaged over mesh surface area, Einstein m^{-2} s^{-1}
$\langle G_j^-\rangle_{A_M}$ = backward incident radiation in j-region averaged over mesh surface area, Einstein m^{-2} s^{-1}
L = length of each j-region, m
M = inert species
Q_j = flow rate at region j, cm^3 min^{-1}
Q = total flow rate entering the reactor, cm^3 min^{-1}
$R^*_{g,j}$ = superficial rate of electron-hole generation at mesh j, mol s^{-1} m^{-2}
$R^*_{g,j+1}$ = superficial rate of electron-hole generation at mesh j+1, mol s^{-1} m^{-2}
R_N = reflectance of a set of N meshes, dimensionless
$\langle R_{TCE}\rangle_{A_{total}}$ = global reaction rate, mol s^{-1} m^{-2}
$[TCE]_0$ = C^0_{TCE} feed concentration of TCE, mg m^{-3}
$[TCE]_j^{exit}$ = $C_{TCE}|_j^{exit}$TCE concentration at the exit of j-region, mg m^{-3}
$[TCE]_{\Sigma j}^{exit}$ = $C_{TCE}|_{\Sigma j}^{exit}$TCE concentration at the exit of the reactor, mg m^{-3}
T_N = transmittance of a set of N meshes, dimensionless

Greek letters

ε_{CM} = fraction of solid coated mesh, dimensionless
λ = wavelength, nm
ϕ = primary quantum yield, mol $Einstein^{-1}$
$\underline{\Omega}$ = unit vector along the ray direction, dimensionless

Literature Cited

1. Fujishima A, Hashimoto K, Watanabe T. *TiO_2 Photocatalysis, Fundamentals and Applications*. Tokyo: Bkc, Inc.;1999.
2. Raupp GB, Nico JA, Annangi S, Changrani R, Annapragada R. Two-flux radiation model for an annular packed-bed photocatalytic reactor. *AIChE J.* 1997;43:792-801.
3. Maruyama T, Nishimoto T. Light intensity profile in heterogeneous photochemical reactor. *Chem Eng Commun.* 1992;117:111-116.
4. Hossain MM, Raupp GB. Radiation field modeling in a photocatalytic monolith reactor. *Chem Eng Sci.* 1998;53:3771-3780.
5. Hossain MM, Raupp GB. Polychromatic radiation field model for a honeycomb monolith photocatalytic reactor. *Chem Eng Sci.* 1999;54: 3027-3034.
6. Changrani RG, Raupp GB. Monte carlo simulation of the radiation field in a reticulated foam photocatalytic reactor. *AIChE J.* 1999;45: 1085-1094.
7. Changrani RG, Raupp GB. Two-dimensional heterogeneous model for a reticulated-foam photocatalytic reactor. *AIChE J.* 2000;46:829-842.
8. Zhang Z, Anderson WA, Moo-Young M. Rigorous modeling of UV absorption by TiO_2 films in a photocatalytic reactor. *AIChE J.* 2000; 46:1461-1470.
9. Esterkin CR, Negro AC, Alfano OM, Cassano AE. Radiation field inside a reactor of glass-fiber meshes coated with TiO_2. *AIChE J.* 2002;48(4):832-845.
10. Dibble LA, Raupp GB. Kinetics of gas-solid heterogeneous photocatalytic oxidation of trichloroethylene by near UV illuminated titanium dioxide. *Catal Lett.* 1990;4:345-354.
11. Upadhya S, Ollis DF. A simple kinetic model for the simultaneous concentration and intensity dependencies of TCE photocatalyzed destruction. *J Adv Oxid Technol.* 1998;3:199-202.
12. Wang K, Tsai H, Hsieh Y. The kinetics of photocatalytic degradation of trichloroethylene in gas-phase over TiO_2 supported on glass bead. *Appl Catal B Environ.* 1998;17:313-320.
13. Amama PB, Itoh K, Murabayashi M. Photocatalytic oxidation of trichloroethylene in humidified atmosphere. *J Mol Catal A: Chem.* 2001;176:165-172.
14. Zhao L, Ozaki S, Itoh K, Murabayashi M. Self-catalytic behavior in gas-phase photocatalytic oxidation of trichloroethylene using TiO_2. *Electrochemistry*. 2002;70:8-12.
15. Kim SB, Hong SC. Kinetic study for photocatalytic degradation of volatile compounds in air using thin film TiO_2 *Photocatalyst Appl Catal B: Environ.* 2002;35:305-315.
16. Amama P, Itoh K, Murabayashi M. Photocatalytic degradation of trichloroethylene in dry and humid atmospheres: role of gas-phase reactions. *J Mol Catal A: Chem.* 2004;217:109-115.
17. Demeestere K, Dewulf J, Van Langenhove H, Sercu B. Gas-solid adsorption of selected volatile organic compounds on titanium dioxide Degussa P25. *Chem Eng Sci.* 2003;58:2255-2267.
18. Demeestere K, De Visscher A, Dewulf J, Van Leeuwen M, Van Langenhove H. A new kinetic model for titanium dioxide mediated heterogeneous photocatalytic degradation of trichloroethylene in gas-phase. *Appl Catal B: Environ.* 2004;54:253-266.
19. Sauer ML, Hale MA, Ollis DF. Heterogeneous photocatalytic oxidation of dilute toluene-chlorocarbon mixtures in air. *J Photochem Photobiol A: Chem.* 1995;88:169-178.
20. Nimlos MR, Jacoby WA, Blake DM, Milne TA. Direct mass spectrometric studies of the destruction of hazardous wastes. 2. Gas-phase photocatalytic oxidation of trichloroethylene over TiO_2: Products and mechanisms. *Environ Sci Technol.* 1993;27:732-740.
21. Siegel R, Howell JR. *Thermal Radiation Heat Transfer*, 3rd Ed. Washington, DC: Hemisphere; 1992.
22. Alfano OM, Cabrera MI, Cassano AE. Photocatalytic reactions involving hydroxyl radical attack. I. Reactions kinetics formulation with explicit photon absorption effects. *J Catal.* 1997;172:370-379.

Manuscript received June 4, 2004, and revision received Nov. 26, 2004.